J. Mech. Phys. Solids 175 (2023) 105286



Contents lists available at ScienceDirect

Journal of the Mechanics and Physics of Solids

journal homepage: www.elsevier.com/locate/jmps





Size-dependent shape characteristics of 2D crystal blisters

Yifan Rao [a], Eunbin Kim [a], Zhaohe Dai [b], Jinlong He [c], Ying Li [c], Nanshu Lu [a,*]

[a] Center for Mechanics of Solids, Structures and Materials, Department of Aerospace Engineering and Engineering Mechanics, The University of Texas at Austin, TX, 78712, United States

[b] Department of Mechanics and Engineering Science, College of Engineering, Peking University, Beijing, 100871, China

[c] Department of Mechanical Engineering, University of Wisconsin-Madison, WI, 53706, United States

ARTICLE INFO

Keywords:
A. Adhesion and adhesives
B. Plates
B. Shells and membranes
V. Variational calculus
2D crystals

ABSTRACT

Micro- and nano-sized blisters can form spontaneously when two-dimensional (2D) crystals are transferred onto substrates because liquid molecules that are initially adsorbed on 2D material and substrate surfaces can be squeezed and trapped by interfacial forces. In this work, we use a combination of experiments, continuum theories, and coarse-grained molecular dynamics (CGMD) simulations to investigate the shape characteristics of spontaneously formed blisters under 2D crystals with heights ranging from a few ångströms to tens of nanometers. We show three distinct regimes in which the height-to-radius ratios (i.e., aspect ratios) of liquid-filled 2D crystal blisters are size-independent, rough linearly proportional, and inversely proportional to the blister radius. We reveal that the blister shape characteristics are governed by three factors: the 2D crystal elasticity, the interfacial interactions, and the phases of confined substances. The characteristic length scales (to which comparing the blister height or radius can define the boundary between these different regimes) are also discussed. We also provide approximate analytical solutions to the blister aspect ratios, which, together with complementary CGMD simulation results, agree with our experimental measurements.

1. Introduction

Two-dimensional (2D) crystals refer to a single layer or a few layers of covalently bonded atoms, including graphene, hexagonal boron-nitride (h-BN), transition metal-dichalcogenides (TMDCs, e.g., MoS_2), among others (Novoselov et al., 2004, 2016; Gibertini et al., 2019). The atomic-level thickness and exceptional mechanical and physical properties of 2D materials make them promising for a wide range of applications, such as flexible and stretchable electronics and photonics (Mak and Shan, 2016; Akinwande et al., 2017; Jang et al., 2022). In most applications, 2D crystals need to be placed on supporting substrates for further fabrication and integration (Geim and Grigorieva, 2013). When 2D crystals interface with another surface, the interfacial van der Waals (vdW) forces squeeze interfacial substances into a blister-shaped volume to lower the system-level energy (Stolyarova et al., 2009; Levy et al., 2010; Sanchez et al., 2021). On the one hand, blisters are undesirable in 2D material devices as they impede charge/photon/phonon transport across the interface, so various means were developed to eliminate interfacial blisters (Uwanno et al., 2015; Pizzocchero et al., 2016; Jain et al., 2018; Purdie et al., 2018; Rosenberger et al., 2018). On the other hand, mechanics analysis has elucidated that the blister morphology is a good indicator of the interfacial properties of 2D crystals, such as adhesion (Khestanova et al., 2016; Sanchez et al., 2018). Furthermore, the inhomogeneous strain distributions and the rich surface topographies of 2D crystal blisters can be leveraged for optimizing luminescence and exciton transport in 2D crystals (De Palma et al., 2020; Brennan et al., 2020) as well as designing mechanical sensors, microlenses, and more (Lin et al., 2020; Yang et al., 2022). Additionally, 2D crystal blisters

* Corresponding author.
E-mail address: nanshulu@utexas.edu (N. Lu).

https://doi.org/10.1016/j.jmps.2023.105286
Received 2 January 2023; Received in revised form 20 March 2023; Accepted 20 March 2023
Available online 24 March 2023
0022-5096/© 2023 Elsevier Ltd. All rights reserved.

can form high-pressure liquid cells for the observation of chemistry under nanoconfinement within transmission electron microscopy (TEM) due to their atomic thinness (Vasu et al., 2016). Therefore, fundamental mechanistic understandings of the spontaneously formed 2D crystal blisters can provide necessary and useful insights for 2D crystal applications.

The 2D crystal blister is a notable example of blistering at thin-film/rigid-substrate interfaces, where crack growth is controlled by balancing the reduction in potential energy with the increase in surface energy in accordance with the Griffith criterion (Griffith, 1921). As a result, self-similarity, i.e., a constant aspect ratio, of blisters at monolayer 2D crystal/substrate interfaces has been widely observed (Khestanova et al., 2016; Sanchez et al., 2018). Their profiles have been quantitatively predicted by considering the competition between the stretching energy of the bulged 2D crystal and the change of interfacial energy. In this scenario, the blister profile features an apparent kink across the blister edge, forming the "contact angle", which is captured by membrane theory (Dai et al., 2018; Blundo et al., 2021; Fang et al., 2022). As the number of 2D crystal layers increases, the bending energy of 2D crystals starts to play a role in the blister morphology (Wang et al., 2022). The blister aspect ratio becomes size-dependent, and the blister edge features a smooth transition to a zero slope, following plate theory (Yue et al., 2012; Wang et al., 2013). The slippage of 2D crystals on substrates also affects the blister morphology (Wang et al., 2017; Dai et al., 2018; Sanchez et al., 2018; Rao et al., 2021). In particular, the hoop compression caused by inward sliding may induce radial wrinkling instabilities (Dai et al., 2020; Dai and Lu, 2021; Ares et al., 2021; Dai et al., 2022).

Although 2D crystal blisters have been investigated from different aspects, the mechanics of 2D crystal blisters with limiting sizes (e.g., a few nm and below) are rather complex (Ares et al., 2021; Dai et al., 2022). There exists a transition between stretching- and bending-dominated blisters (Ma et al., 2022). Moreover, instead of a discontinuity in interfacial energy across the blister edge, continuous vdW interactions have to be considered for these ultra-shallow blisters. The vdW interactions can be viewed as nonlinear elastic springs acting between 2D crystals and substrates (Aitken and Huang, 2010; Gao and Huang, 2011; Xue et al., 2022). It is therefore natural to ask: how large is the vdW process zone, and when should it be incorporated into 2D crystal blister models? Unfortunately, quantitative answers are lacking in existing work. Furthermore, recent studies have indicated that as the blister height approaches a few ångströms, a minimum blister height corresponding to a single molecular layer of interfacial substances emerges, as observed in both experimental studies and molecular dynamics (MD) simulations of 2D crystal blisters (Lee et al., 2012; Iakovlev et al., 2017; Bampoulis et al., 2018; Villarreal et al., 2021). It is therefore interesting to investigate the breakdown of continuum mechanics for ultra-shallow blisters.

Driven by the aforementioned curiosities, we carry out experimental, analytical, and MD investigations on micro- and nano-sized blisters formed by 2D crystals. This paper is organized as follows. In Section 2, we report the experimental procedures for creating parent-satellite blisters at the interface between multilayer graphene (MLG) and silicon-dioxide (SiO_2) substrate. We then establish a Griffith-type model (GTM) in Section 3 to elucidate the spontaneous formation of blisters governed by the competition among the stretching and bending energies of the bulged 2D crystal, the change of interfacial energy, and the interfacial sliding. The GTM predicted aspect ratios agree well with the experimental measurements on the parent blisters but not the satellite ones. Therefore, we establish a cohesive zone model (CZM) to account for the continuous vdW interactions between the bulged 2D crystal and the substrate in Section 4. When the CZM hits a limit of minimum blister size, we leverage coarse-grained molecular dynamics (CGMD) simulations in Section 4 to illustrate a monolayer lattice of confined liquids trapped in ultra-shallow blisters with heights of only a few ångströms. We conclude with a summary of the main findings in Section 5.

2. Experiments and results

2.1. Sample fabrication

We used a standard mechanical exfoliation process (Novoselov and Neto, 2012; Yi and Shen, 2015) to fabricate blisters under 2D crystals. Fig. 1a shows the schematics of the fabrication process. Firstly, large graphite flakes were peeled off from bulk natural graphite (NG) crystals using blue polyethylene cleanroom tapes (CRTs). After repeating the exfoliation process three more times, the exfoliated NG flakes on CRTs were stored in the ambient for at least three hours to collect surface adsorbates. Next, a 300-nm silicon dioxide (SiO_2) on a Si wafer (SQI Inc., Item No. 20040830) was cleaned by sonication with acetone, isopropyl alcohol (IPA), and deionized (DI) water. The SiO_2/Si chip was further soaked in piranha solution (2:1 solution of 67% sulfuric acid and 30% hydrogen peroxide) for five minutes and rinsed with DI water. Immediately after piranha cleaning, the NG flake on CRT was placed on the surface of the cleaned SiO_2/Si chip. Before exfoliating the CRT, the sample was placed on a hot plate (preheated to 100 °C) for two minutes and then cooled down to room temperature naturally. Finally, 2D crystal blisters formed spontaneously at the MLG/SiO_2 interfaces with the removal of the top CRT.

2.2. Shape characterization of 2D crystal blisters

Under an optical microscope, we first identified a flake full of blisters. We then used atomic force microscopy (AFM) (Keyence VK-X1100) to characterize the step height of the flake to be around 3.87 nm, which corresponds to eleven-layer graphene (11LG). The AFM morphology of this 11LG flake is shown in Fig. 1b-(i), and the magnified views of the framed regions are provided in Fig. 1b-(ii)~(iv). In these magnified views, we observed a bunch of unique parent-satellite blister patterns, where many satellite nanoblisters surround a parent microblister. Fig. 1c displays the AFM images of a single parent-satellite blister system on both Day 0 and Day 100 after fabrication. The corresponding AFM height profiles along the longest and the shortest axes of the parent blister are plotted in Fig. 1d. It is evident that this blister stayed almost unchanged over the course of 100 days, which suggests the blister

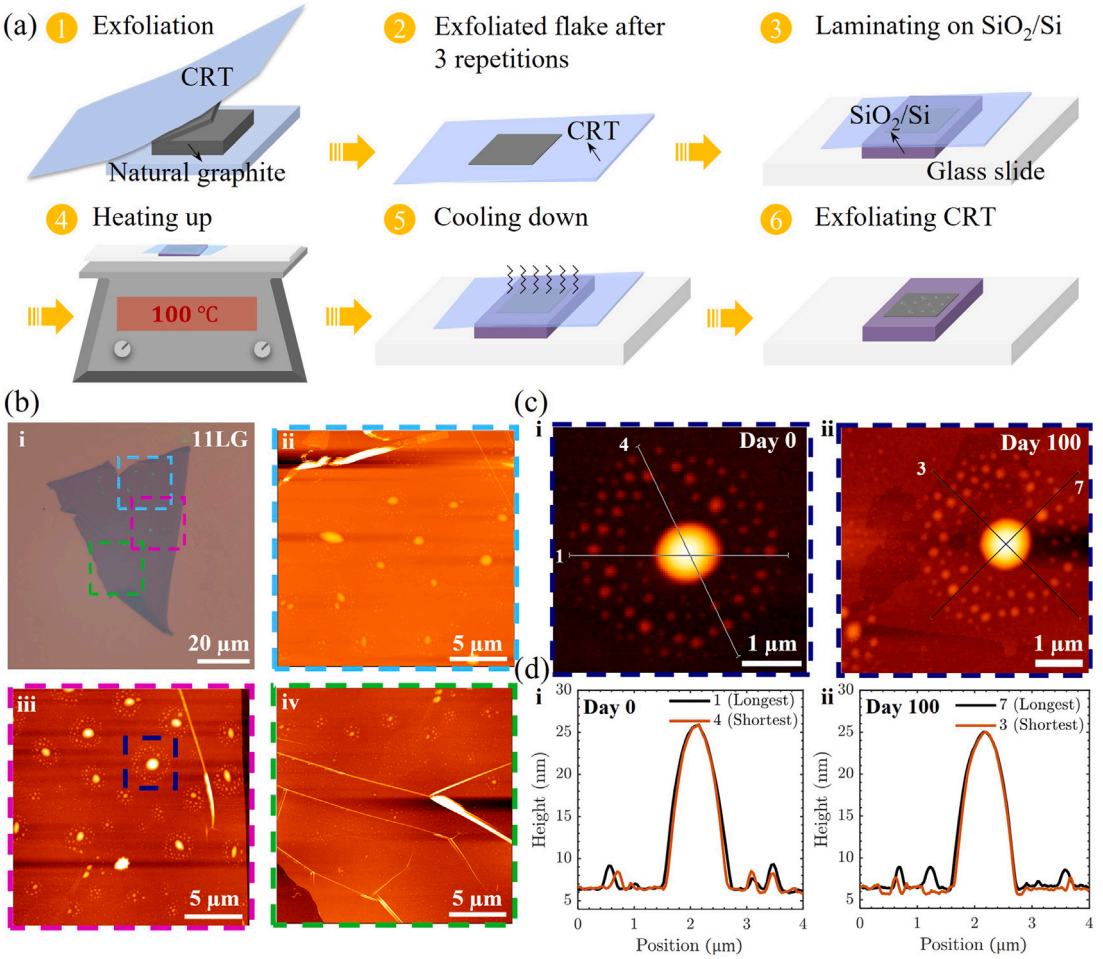


Fig. 1. (a) Schematics of the fabrication process to produce interfacial blisters after exfoliating multilayer graphene (MLG) on a silicon-dioxide (SiO_2) substrate: exfoliate natural graphite (NG) with the aid of blue polyethylene cleanroom tapes (CRTs) (Step 1); repeat the exfoliation process three more times, and then store the exfoliated NG flakes in the ambient for at least three hours (Step 2); place the exfoliated NG flakes on the surface of a cleaned SiO_2/Si chip (Step 3); heat the sample on a hot plate at 100 °C for two minutes (Step 4); cool the sample down to room temperature (Step 5); after peeling off the CRT, blisters form spontaneously at the MLG/SiO_2 interfaces (Step 6). (b) (i) AFM image of eleven-layer graphene (11LG) on SiO_2 substrate immediately after fabrication, and magnified views of (ii) cyan, (iii) magenta, and (iv) green framed regions in (i). (c) AFM images of a single parent-satellite blister system within the blue framed region in (b)-(iii) on (i) Day 0 and (ii) Day 100 after fabrication. (d) AFM height profiles along the longest and the shortest axes of the parent blister on (i) Day 0 and (ii) Day 100 after fabrication. The corresponding orientations of cuts are labeled in (c).

is filled with liquid instead of gas because gas-filled blisters deflate over the course of hours (Lloyd et al., 2017; Sanchez et al., 2018). Additionally, the AFM height profiles along the longest and the shortest axes of the parent blister are almost identical in Fig. 1d, which suggests a round shape of this spontaneously formed interfacial blister. The determination of the directions of the longest and the shortest axes of the parent blister is given in Fig. A.1 (see Appendix A).

Fig. 2a displays the experimentally measured profiles of multiple parent (blue stars) and satellite (red circles) blisters appearing in Fig. 1b-(iii) after normalizing the deflection z by the blister central height h and the radial position r by the blister radius a. Based on previous mechanics research (Yue et al., 2012; Wang et al., 2013; Dai et al., 2018; Sanchez et al., 2018), we present a generic form for the normalized profile function of 2D crystal blisters:

$$\frac{z}{h} = \left[1 - \left(\frac{r}{a}\right)^p\right]^q. \tag{1}$$

Here, $\{p = 2, q = 2\}$ represents a bulged plate shape in the plate limit, where the blister edge is depicted as a smooth transition to zero slopes across the edge (see the solid curve in Fig. 2a). On the other hand, $\{p = 2, q = 1\}$ represents a bulged membrane shape in the membrane limit, where the blister edge is depicted as a kink with a well-defined contact angle (see the dashed curve in Fig. 2a). More recent work has numerically demonstrated that $p \simeq 2.2$ fits better for bulged membrane-like blisters with $h/a > 0.01$ (Blundo et al., 2021). However, by comparing to the experimental data, we find that Eq. (1) with $\{p = 2, q = 1\}$ better fits the experimentally measured parent blister profiles in our 11LG/SiO_2 interface system. Comparing the experimental markers with the analytical curves,

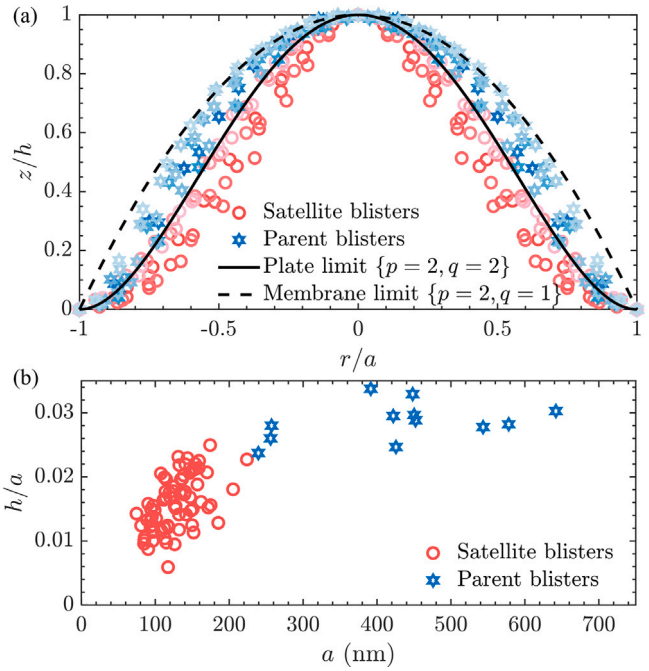


Fig. 2. (a) Normalized height profiles of multiple parent (blue stars) and satellite (red circles) blisters in Fig. 1b-(iii). Here, the central heights of satellite blisters vary from 0.9 nm to 3.4 nm, and the central heights of parent blisters vary from 6.8 nm to 19.5 nm. The color of the circles/stars fades as the central height enlarges. The dashed and solid curves correspond to a bulged membrane shape (Eq. (1) with $\{p = 2, q = 1\}$) and a bulged plate shape (Eq. (1) with $\{p = 2, q = 2\}$), respectively. (b) Aspect ratio vs. blister radius obtained by experiments.

we can discover that the parent blister profiles transition from bulged plate to bulged membrane as the central height increases from 6.8 nm to 19.5 nm. In contrast, while the plate limit can capture the taller satellite blisters, it overestimates the deflections for ultra-shallow blisters ($h \lesssim 3$ nm).

Besides the profile function, the aspect ratio is also employed to characterize the shape of 2D crystal blisters. Fig. 2b presents the relationship between the aspect ratio and the blister radius for both parent and satellite blisters, as determined from experimental measurements. It is apparent that the aspect ratio of parent blisters is nearly independent of size, while that of satellite blisters depends on size. A comprehensive theoretical framework is required to fully elucidate the mechanics underlying these shape characteristics for 2D crystal blisters of varying heights, extending down to ångström scales.

3. Griffith-type model (GTM)

In this section, we assess the variation of interfacial energy during blistering by employing a uniform intensity (i.e., the change of interfacial energy per unit area $\Delta\gamma$) (Griffith, 1921). A Griffith-type model (GTM) is subsequently established to elucidate the shape characteristics of 2D crystal blisters, which are governed by the competition among the stretching and bending energies of the bulged 2D crystal, the change of interfacial energy, and the interfacial sliding.

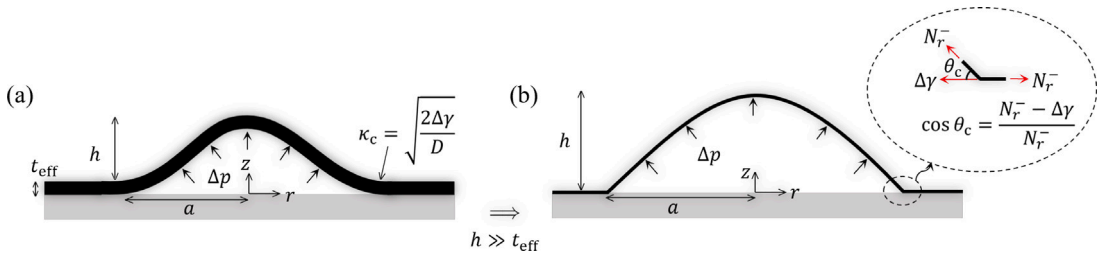


Fig. 3. Schematic illustration and notations for the Griffith-type model (GTM) of 2D crystal blisters. (a) A bulged plate-like profile with $h \lesssim O(t_{\text{eff}})$. Here, a discontinuous curvature κ_c across the blister edge is characterized by GTM. (b) A bulged membrane-like profile with $h \gg t_{\text{eff}}$. Here, a discontinuous slope across the blister edge ("critical contact angle" θ_c) is characterized by GTM. The determination of θ_c is based on a force balance at the contact line, as illustrated in the enlarged view. $\Delta\gamma$, D, and N_r^- represent the change of interfacial energy per unit area, the bending stiffness, and the radial membrane tension evaluated at the inner side of $r = a$, respectively.

3.1. Scaling analysis

We begin by performing a scaling analysis to estimate the stretching and bending energies of bulged 2D crystals, as well as the change of interfacial energy during blistering. The stretching energy of bulged 2D crystals is estimated by $U_s \sim E_{2D}\epsilon^2 a^2$ where $E_{2D} = Et$ is the in-plane Young's modulus, E is the Young's modulus, t is the 2D crystal thickness, and $\epsilon \sim h^2/a^2$ is the typical sheet strain. The bending energy of bulged 2D crystals is estimated by $U_b \sim D\kappa^2 a^2$ where D is the bending stiffness and $\kappa \sim h/a^2$ is the typical sheet curvature. The change of interfacial energy during blistering is estimated by $\phi_i \sim \Delta\gamma a^2$.

Comparing the bending energy to the stretching energy, $U_b/U_s \sim (t_{\text{eff}}/h)^2$, where $t_{\text{eff}} = \sqrt{D/E_{2D}}$ is the "effective" thickness, elucidates the significance of the bendability of 2D sheets. This result suggests that the bulged 2D crystal is stretching-dominated when $h \gg t_{\text{eff}}$ while bending-dominated when $h \lesssim O(t_{\text{eff}})$. Fig. 3 sketches the bulged plate-like profile with $h \lesssim O(t_{\text{eff}})$ and the bulged membrane-like profile with $h \gg t_{\text{eff}}$, respectively.

Next, the equilibrium state of spontaneously formed interfacial blisters is captured by minimizing the total free energy $(U_s + U_b + \phi_i)$ with respect to arbitrary a. Therefore, in the membrane limit, $\partial(U_s + \phi_i)/\partial a = 0$, which leads to $h/a \sim (\Delta\gamma/E_{2D})^{1/4}$; in the plate limit, $\partial(U_b + \phi_i)/\partial a = 0$, which leads to $h/a \sim (\Delta\gamma/D)^{1/2}a$. It indicates that the aspect ratio is size-independent for stretching-dominated blisters but linearly proportional to the blister radius for bending-dominated blisters. Fig. 2b shows the aspect ratio-blister radius relationship obtained from experiments, which suggests that the parent blisters are stretching-dominated while the satellite blisters are bending-dominated.

The slippage of 2D crystals on substrates also affects blister morphology (Wang et al., 2017; Dai et al., 2018; Sanchez et al., 2018; Rao et al., 2021). In particular, radially inward sliding of the 2D sheet can cause hoop compression, which can induce wrinkling instability (Dai et al., 2020; Ares et al., 2021; Dai and Lu, 2021). In our recent work (Dai et al., 2022), we proposed a sliding number defined as

$$S_{\text{ea}} = \frac{\sqrt{E_{2D}\Delta\gamma}}{\tau a}, \tag{2}$$

where τ represents the uniform shear stress at the 2D crystal/substrate interface. For the 11LG/SiO_2 interface, $S_{\text{ea}} \sim O(10^2)$ since $E_{2D} \approx 3806$ N/m, $\Delta\gamma \approx 0.01$ N/m, and $\tau \approx 1$ MPa (Sanchez et al., 2018). The interfacial shear becomes negligible, and the 11LG/SiO_2 interface is characterized as frictionless as a result of $S_{\text{ea}} \gg 1$. Furthermore, since no wrinkles were observed in either the attached or suspended areas of each blister (see Fig. 1c), we exclude the possibility of wrinkling instability caused by the interfacial sliding from this work.

3.2. Equilibrium equations

To unveil the mechanics of 2D crystal blisters, a polar coordinates system (r, z) is established at the neutral plane of 2D sheets before bulging (see Fig. 3). After bulging, the radial displacement and the vertical deflection at an arbitrary position of the neutral plane can be denoted by $u(r)$ and $w(r)$, respectively. Therefore, the radial and the hoop membrane strains are defined by

$$\begin{cases} \epsilon_r = u' + \frac{1}{2}w'^2 \\ \epsilon_\theta = \frac{u}{r} \end{cases}, \tag{3}$$

where $()'$ denotes $\frac{\mathrm{d}}{\mathrm{d}r}$.

Next, the Airy stress function $\psi(r)$ is introduced to denote the radial and the hoop membrane tensions, leading to

$$\begin{cases} N_r = \frac{\psi'}{r} \\ N_\theta = \psi'' \end{cases}, \tag{4}$$

where $()''$ denotes $\frac{\mathrm{d}^2}{\mathrm{d}r^2}$. Notably, the in-plane equilibrium of the bulged 2D crystal is inherently satisfied by Eq. (4). Besides, a linear constitutive law is adopted here since the typical strain of the bulged 2D crystal is quite small (i.e., $\epsilon \propto (h/a)^2 \sim o(10^{-3})$, see Fig. 2b). Thus, one obtains

$$\begin{cases} N_r = \frac{E_{2D}}{1-\nu^2}(\epsilon_r + \nu\epsilon_\theta) \\ N_\theta = \frac{E_{2D}}{1-\nu^2}(\epsilon_\theta + \nu\epsilon_r) \end{cases}, \tag{5}$$

where ν is Poisson's ratio.

Furthermore, the out-of-plane equilibrium of the bulged 2D crystal can be described by the Föppl-von Kármán (Fvk) equation (Mansfield, 2005), expressed as

$$\nabla^2(D\nabla^2 w) - [\psi, w] - \Delta p = 0, \tag{6}$$

where $\nabla^2 f = \frac{\mathrm{d}^2 f}{\mathrm{d}r^2} + \frac{1}{r}\frac{\mathrm{d}f}{\mathrm{d}r}$, $[f, g] = \frac{1}{r}\frac{\mathrm{d}}{\mathrm{d}r}(\frac{\mathrm{d}f}{\mathrm{d}r}\frac{\mathrm{d}g}{\mathrm{d}r})$, and Δp is the pressure difference across the bulged 2D crystal due to the incompressibility of confined liquids.

In addition, the compatibility of strains requires the following relation:

$$\nabla^4\psi + \frac{E_{2D}}{2}[w, w] = 0, \tag{7}$$

where $\nabla^4 f = \nabla^2\nabla^2 f$.

3.3. Adhesive boundary conditions

Previous studies have demonstrated that in the membrane limit ($h \gg t_{\mathrm{eff}}$), the critical contact angle at the blister edge can be described by (Rao et al., 2021; Dai et al., 2022)

$$\cos\theta_{\mathrm{c}} = \frac{N_r^- - \Delta\gamma}{N_r^-}, \tag{8}$$

where N_r^- denotes the radial membrane tension at the inner side of $r = a$. It is worth noting that at the frictionless interface, both displacements and membrane tensions remain continuous across the blister edge. Hence, according to Eq. (8), it can be inferred that θ_{c} is determined by a force balance at the contact line, as illustrated in the enlarged view of Fig. 3b.

As the number of 2D crystal layers increases, bending energy starts to influence the blister morphology. To account for this, a similar energy analysis considering bending energy was conducted in Appendix B, resulting in a modified adhesive boundary condition at the frictionless interface, which reads

$$\frac{1}{2}D[w''(a^-)]^2 = \Delta\gamma, \tag{9}$$

where a^- represents the inner side of $r = a$. This equation suggests the existence of a critical curvature $\kappa_{\mathrm{c}} = \sqrt{2\Delta\gamma/D}$ across the blister edge (see Fig. 3a). A supplementary equation is also introduced through the energy analysis to ensure the kinematic admissibility of the deformation of 2D sheets:

$$N_r^- + N_\theta^- = 0, \tag{10}$$

where N_θ^- represents the hoop membrane tension evaluated at the inner side of $r = a$.

3.4. Numerical method

We introduce non-dimensionalization below to facilitate the solution of GTM. Since the radius a is not known prior, we use the effective thickness $t_{\mathrm{eff}} = \sqrt{D/E_{2\mathrm{D}}}$ to rescale the system:

$$R = \frac{r}{t_{\mathrm{eff}}}, U = \frac{u}{t_{\mathrm{eff}}}, W = \frac{w}{t_{\mathrm{eff}}}, R_a = \frac{a}{t_{\mathrm{eff}}}, \Psi = \frac{\psi}{D}, \bar{P} = \frac{\Delta p t_{\mathrm{eff}}^3}{D}. \tag{11}$$

Next, we integrate the governing Eqs. (6) and (7) with respect to r, and then, with the aid of Eq. (11), we rescale the governing equations of GTM as

$$\begin{cases} W''' + \frac{W''}{R} - \frac{W'}{R^2} - \frac{\Psi' W'}{R} - \frac{\bar{P}R}{2} = 0 \\ R\Psi''' + \Psi'' - \frac{\Psi'}{R} + \frac{W'^2}{2} = 0 \end{cases}. \tag{12}$$

In addition, three boundary conditions arise naturally with the aid of Eqs. (3)–(5), which are written as

$$\begin{cases} u(0) = \frac{1}{E_{2\mathrm{D}}}(\psi''(r) - \nu\frac{\psi'(r)}{r})|_{r=0} = 0 \\ w'(0) = 0 \\ w'(a) = 0 \end{cases}. \tag{13}$$

Following the nondimensionalization given by Eq. (11), the rescaled form of all boundary conditions Eqs. (9), (10), and (13) reads

$$\begin{cases} \Psi''(R) - \nu\frac{\Psi'(R)}{R}|_{R=0} = 0 \\ W'(0) = 0 \\ W'(R_a) = 0 \\ [W''(R_a)]^2 = 2\eta \\ \Psi''(R_a) + \frac{\Psi'(R_a)}{R_a} = 0 \end{cases}, \tag{14}$$

where $\eta = \Delta\gamma/E_{2\mathrm{D}}$ is the adhesive number that characterizes the intensity of interfacial energy relative to the in-plane stiffness of 2D crystals. Eqs. (12) and (14) give a comprehensive description of the boundary value problem (BVP) regarding 2D crystal blisters at the frictionless interface based on GTM, which can be numerically solved by the built-in solver bvp4c in MATLAB.

3.5. Approximate analytical solutions

Based on the linear plate theory and the principle of minimum energy, earlier work (Yue et al., 2012) derived the change of interfacial energy per unit area during blistering as

$$\Delta\gamma = \frac{32Dh^2}{a^4} \tag{15}$$

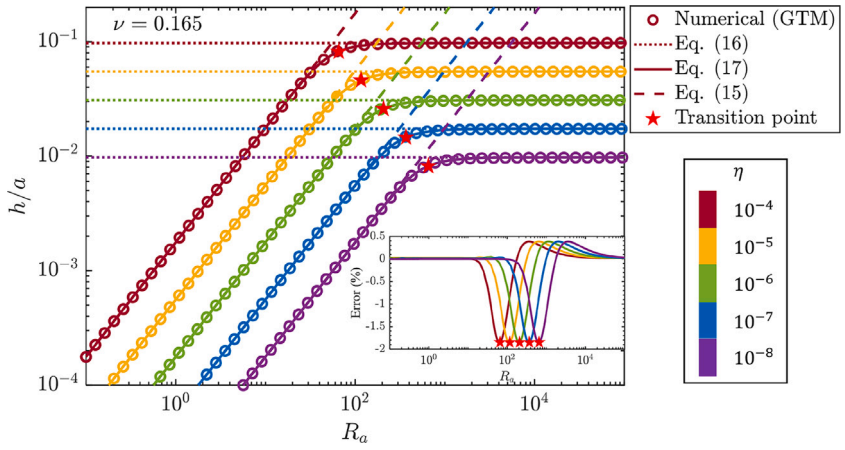


Fig. 4. Aspect ratio vs. normalized blister radius under various adhesive numbers η. Circles are numerical solutions to GTM; dashed and dotted lines are asymptotic solutions to GTM based on membrane and plate theories, respectively; solid curves are the approximate analytical solutions given by Eq. (17). Red stars highlight the transition points from plate-like behavior to membrane-like behavior. The inset shows the error between the numerical results and the approximate solutions.

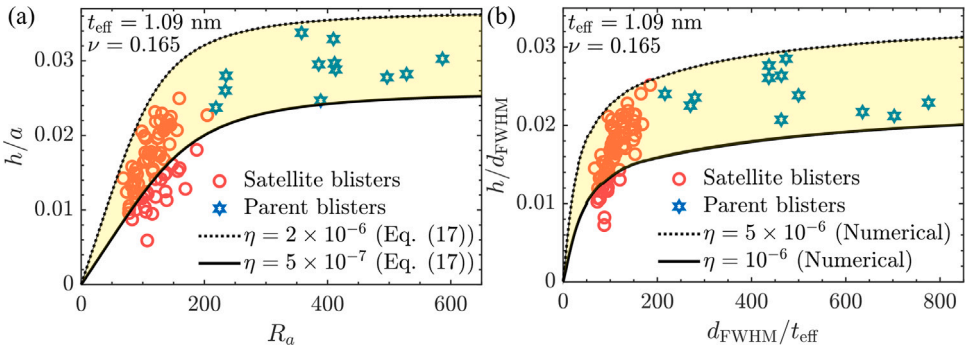


Fig. 5. (a) Aspect ratio vs. normalized radius obtained by both experiments (hollow circles/stars) and approximate solutions to GTM (solid and dashed curves). η is the adhesive number that appeared in Eq. (14). (b) Height normalized by the full width at the half of maximum height (FWHM) (d_{FWHM}) vs. normalized d_{FWHM} obtained by both experiments (hollow circles/stars) and numerical solutions to GTM (solid and dashed curves).

in the plate limit. However, in the membrane limit, such an exact solution does not exist. Scaling analysis in Section 3.1 suggests $\Delta\gamma \propto E_{2D}h^4/a^4$. The approach to solving the BVP built in Section 3.4 allows us to numerically extract the prefactor of this formula, which leads to

$$\Delta\gamma \approx \frac{1.108E_{2D}h^4}{a^4}. \tag{16}$$

This prefactor value has also been determined in our recent work (Dai et al., 2022), which is slightly smaller than the value of 1.13 estimated by Khestanova et al. (2016) and larger than the value of 5/6 obtained analytically by Sanchez et al. (2018). Notably, the details of extracting the prefactor can be found in Appendix C.

The superposition of Eqs. (15) and (16) provides an approximate analytical solution for 2D crystal blisters at the frictionless interface, which is written as

$$\Delta\gamma = \frac{32Dh^2}{a^4} + \frac{1.108E_{2D}h^4}{a^4}. \tag{17}$$

3.6. Results and discussions

Fig. 4 compares the approximate solutions given by Eq. (17) with the numerical solutions to GTM. The inset shows the error between the two solutions, defined by the percentage difference in the solutions: Error (%) = (approximate solution/numerical result−1) × 100 (%). The plot reveals that the maximum error is no more than 2% for various η, indicating good agreement between the approximate solutions and numerical results. Moreover, the asymptotic solutions given by Eqs. (15)–(16) agree well with the numerical solutions to GTM in the plate and the membrane limits, respectively. Therefore, it can be concluded that, according to

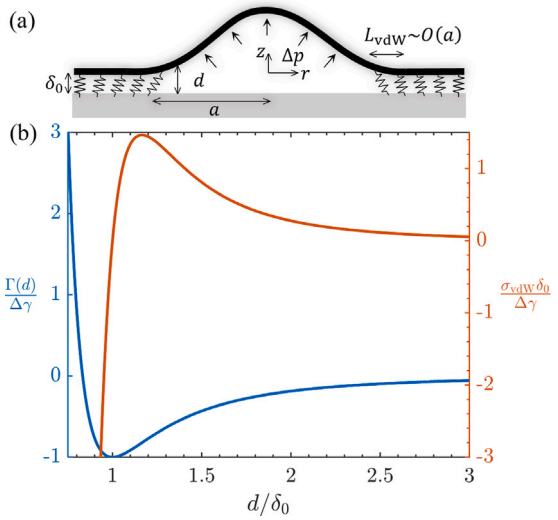


Fig. 6. (a) Schematic illustration and notations for the cohesive zone model (CZM) of 2D crystal blisters. δ_0 denotes the equilibrium vdW distance. The vdW length scale is specified as $L_{vdW} = (D\delta_0^2/\Delta\gamma)^{1/4}$. (b) The variation of normalized vdW potential (the blue curve) and normalized vdW stress (the red curve) with respect to the normalized interfacial distance.

GTM, the aspect ratio of 2D crystal blisters is linearly proportional to the blister radius in the plate limit while size-independent in the membrane limit.

To determine the criterion for the plate-to-membrane transition, the term related to bending energy and the term related to stretching energy in Eq. (17) are equated. This leads to the critical central height (h_t) and the critical radius (a_t), given by

$$\begin{cases} h_t \approx 5.374 t_{eff} \\ a_t \approx 6.557 \eta^{-1/4} t_{eff} \end{cases}. \tag{18}$$

The insert of Fig. 4 illustrates that the points where the plate-to-membrane transition occurs (labeled by red stars) are in agreement with the locations of the maximum errors. According to Eq. (18), we conclude that the profile of a 2D crystal blister is plate-like when $h < 5.374 t_{eff}$ and membrane-like when $h > 5.374 t_{eff}$.

Next, we provide details on the mechanical and interfacial properties of the 11LG/SiO_2 sample, enabling a comparison between the results of GTM and experimental measurements. The Young's modulus of the sample is set to $E = 1$ TPa, the distance between two graphene layers is $d_0 = 0.346$ nm, the number of graphene layers is $N = 11$, the in-plane Young's modulus is $E_{2D} = NEd_0 = 3806$ N/m, Poisson's ratio is $\nu = 0.165$, and the bending stiffness is determined by (Koskinen and Kit, 2010)

$$D = N D_s + E d_0^3 (N^3 - N)/12, \tag{19}$$

where $D_s = 1.6$ ev is the bending stiffness of monolayer graphene. The effective thickness of 11LG is then calculated to be $t_{eff} \approx 1.09$ nm.

Fig. 5a presents the aspect ratio-normalized radius relationship as predicted by the analytical approximations and experiments. To account for the scatter in experimental data, we analyze two different adhesive numbers, $\eta = 2 \times 10^{-6}$ and $\eta = 5 \times 10^{-7}$, to capture the upper and lower limits of aspect ratios of parent blisters measured in experiments, respectively. However, we note that the experimental data for satellite blisters deviate from the yellow-shaded region bounded by the two analytical limits. To avoid attributing the deviation solely to measurement errors, we measure the full width at half maximum height (FWHM) (d_{FWHM}) instead of the blister radius. A more significant discrepancy between the numerical solutions to GTM and the experimental data for satellite blisters can be observed in Fig. 5b, which shows h/d_{FWHM}-normalized d_{FWHM} relationships. To account for the discrepancy, we introduce continuous vdW interactions between 2D crystals and substrates to our theoretical model in the following section.

4. Cohesive zone model (CZM)

4.1. Process zone of van der Waals interactions

The cohesive zone model (CZM) is distinct from the GTM in that it postulates a finite-sized "process zone" of vdW interactions, rather than an "interfacial energy density jump" $\Delta\gamma$ across the blister edge. As shown in Fig. 6a, the continuous vdW interactions are modeled as an array of nonlinear elastic springs acting between 2D crystals and substrates. To quantify the pairwise interaction between an atom in the 2D crystal and its substrate, we use a standard form of the Lennard-Jones potential. The adhesive potential

(per unit area) between the graphene sheet and the substrate, which comprises both vdW attraction and Born repulsion, is given by (Aitken and Huang, 2010; Gao and Huang, 2011)

$$\Gamma(d) = -\Delta\gamma\left[\frac{3}{2}\left(\frac{\delta_0}{d}\right)^3 - \frac{1}{2}\left(\frac{\delta_0}{d}\right)^9\right], \tag{20}$$

where δ_0 represents the equilibrium distance between the bottom layer of 2D crystal and the substrate, where the vdW potential function reaches its minimum value at $d = \delta_0$ (see the blue curve in Fig. 6b), and d denotes the distance between an arbitrary point on the 2D crystal and the substrate, such that $d = \delta_0 + w$. It is important to note that $\Delta\gamma$ of the CZM has exactly the same physical meaning as the GTM, namely, the change of interfacial energy per unit area during blistering.

The vdW stress (per unit area, positive for attraction) is then written as

$$\sigma_{\mathrm{vdW}}(d) = \frac{9\Delta\gamma}{2\delta_0}\left[\left(\frac{\delta_0}{d}\right)^4 - \left(\frac{\delta_0}{d}\right)^{10}\right], \tag{21}$$

which is the first derivative of the vdW potential $\Gamma(d)$ with respect to d. The red curve in Fig. 6b presents the distributions of vdW stress with respect to the normalized interfacial distance. For ultra-shallow and bending-dominated blisters, the distance d is approximately equal to the blister height h and on the order of the equilibrium distance δ_0, i.e., $d \sim h \sim O(\delta_0)$. This yields $\Delta\gamma \sim Dh^2/a^4 \sim D\delta_0^2/a^4$. Consequently, a vdW length scale $L_{\mathrm{vdW}} = (D\delta_0^2/\Delta\gamma)^{1/4}$ is derived to access the importance of the size of vdW process zone. As depicted in Fig. 6a, the vdW process zone becomes significant when $a \lesssim O(L_{\mathrm{vdW}})$, and negligible otherwise.

4.2. General formulation

When considering the distributed vdW stress, the governing equations of 2D crystal blisters are written as

$$\begin{cases} \nabla^2(D\nabla^2 w) - [\psi, w] + \sigma_{\mathrm{vdW}} - \Delta p\mathcal{H}(r-a) = 0 \\ \nabla^4\psi + \frac{E_{2\mathrm{D}}}{2}[w, w] = 0 \end{cases}, \tag{22}$$

where $\mathcal{H}(x) = 1$ for $x < 0$ and 0 otherwise. The following non-dimensionalization is then introduced to the CZM:

$$\begin{aligned} \hat{U} = \frac{u}{L_{\mathrm{vdW}}}, \hat{R} = \frac{r}{L_{\mathrm{vdW}}}, \lambda = \frac{a}{L_{\mathrm{vdW}}}, D_{\mathrm{FWHM}} = \frac{d_{\mathrm{FWHM}}}{L_{\mathrm{vdW}}}, \\ \hat{W} = \frac{w}{\delta_0}, H = \frac{w(0)}{\delta_0}, T_{\mathrm{eff}} = \frac{t_{\mathrm{eff}}}{\delta_0}, \\ \hat{\Psi} = \frac{\psi}{D}, \hat{P} = \frac{\Delta p\delta_0}{\Delta\gamma}, \hat{\sigma}_{\mathrm{vdW}} = \frac{\sigma_{\mathrm{vdW}}\delta_0}{\Delta\gamma}. \end{aligned} \tag{23}$$

Here, $\delta_0 = 0.4$ nm is used in this work (Gupta et al., 2006; Ishigami et al., 2007; Sonde et al., 2009). Using Eqs. (23), (22) is rescaled as

$$\begin{cases} \hat{W}'''' + \frac{2\hat{W}'''}{\hat{R}} - \frac{\hat{W}''}{\hat{R}^2} + \frac{\hat{W}'}{\hat{R}^3} - \frac{\hat{\Psi}'\hat{W}''}{\hat{R}} - \frac{\hat{\Psi}''\hat{W}'}{\hat{R}} + \frac{9}{2}[(\frac{1}{\hat{W}+1})^4 - (\frac{1}{\hat{W}+1})^{10}] - \hat{P}\mathcal{H}(\hat{R}-\lambda) = 0 \\ \hat{R}\hat{\Psi}''' + \hat{\Psi}'' - \frac{\hat{\Psi}'}{\hat{R}} + \frac{\hat{W}'^2}{2T_{\mathrm{eff}}^2} = 0 \end{cases}. \tag{24}$$

Furthermore, the set of continuous conditions at $\hat{R} = \lambda$ are given by

$$[\![\hat{\Psi}']\!] = [\![\hat{\Psi}'']\!] = [\![W]\!] = [\![W'']\!] = [\![W''']\!] = 0, \tag{25}$$

where $[\![f]\!] = f(\lambda^+) - f(\lambda^-)$. Besides, the complete set of boundary conditions for the CZM are as follows

$$\begin{cases} \hat{\Psi}''(\hat{R}) - \nu\frac{\hat{\Psi}'(\hat{R})}{\hat{R}}|_{\hat{R}=0} = 0 \\ \frac{\hat{W}'(\hat{R})}{\hat{R}} - \hat{W}''(\hat{R})|_{\hat{R}=0} = 0 \\ \hat{W}'''(0) = 0 \\ \hat{W}(\lambda) = 0 \\ \hat{W}(\infty) = 0 \\ \hat{W}'(\infty) = 0 \\ \hat{\Psi}''(\hat{R}) - \nu\frac{\hat{\Psi}'(\hat{R})}{\hat{R}}|_{\hat{R}=\infty} = 0 \end{cases}. \tag{26}$$

Eqs. (24)–(26) provide a closed form solution for the BVP based on the CZM, which can be numerically solved using the built-in solver bvp4c in MATLAB. However, the highly nonlinear nature of this BVP makes it challenging to find numerical solutions for ultra-shallow blisters with heights of a few ångströms (Wang et al., 2016). To gain a better understanding of the mechanics of ultra-shallow blisters, coarse-grained molecular dynamics (CGMD) simulations based on the CZM were also performed. Details of these simulations can be found in Appendix D.

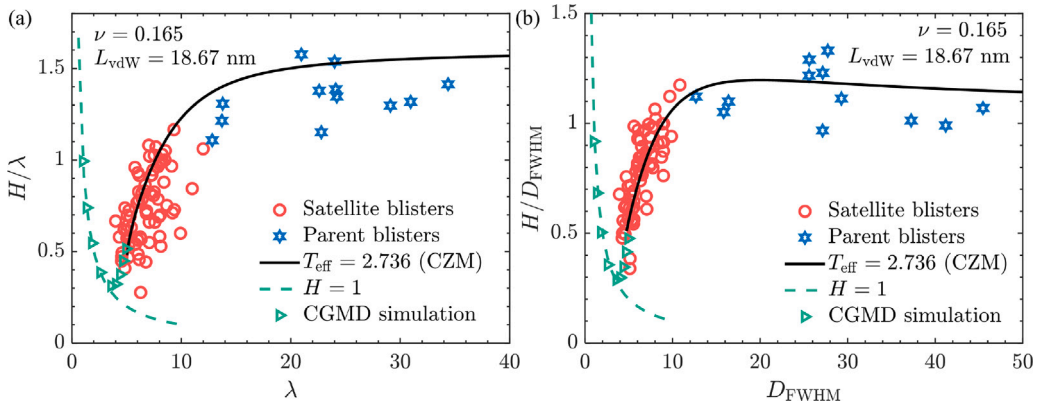


Fig. 7. (a) Normalized aspect ratio vs. normalized radius and (b) the ratio of normalized height to normalized full width at the half of maximum height (FWHM) (D_{FWHM}) vs. D_{FWHM}. In both plots, hollow circles/stars represent experimental measurements, black curves are the numerical solutions to CZM, and green triangles come from CGMD simulations. The green dashed curve indicates a reciprocal relation with $H = 1$.

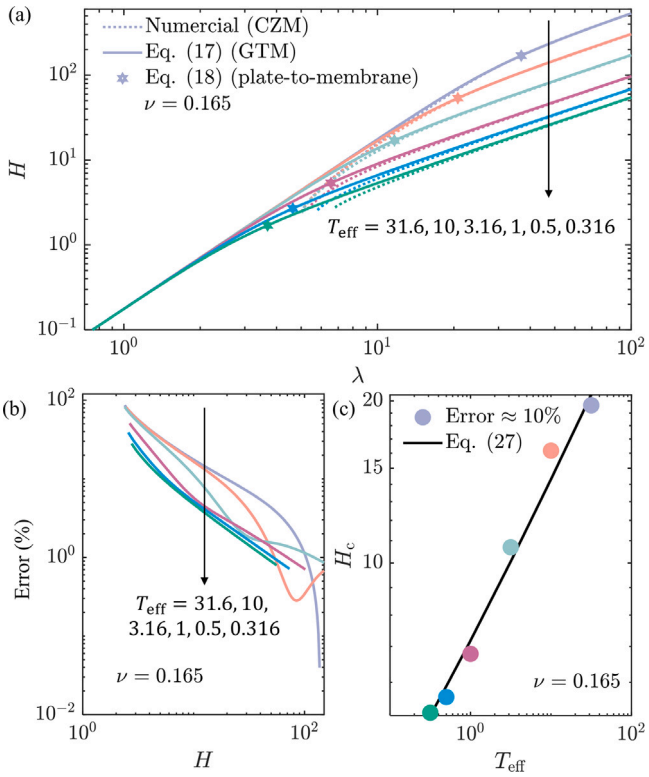


Fig. 8. (a) Normalized height vs. normalized radius under various T_{eff} given by numerical solutions to CZM and approximate solutions to GTM. (b) The error between numerical solutions to CZM and approximate solutions to GTM with respect to the normalized height under various T_{eff}. (c) The normalized critical heights for the GTM-to-CZM transition vs. T_{eff}. The black curve is a fitted line given by Eq. (27).

4.3. Results and discussions

Fig. 7 presents a comparison between the numerical solutions to CZM and experimental measurements. It is worth noting that the value of $\Delta\gamma$ used here is 6×10^{-3} N/m, which results in $L_{vdW} \approx 18.67$ nm. The good agreement shown in Fig. 7b indicates that, aside from the plate-like behavior, the distribution of interfacial interactions is crucial in determining the morphology of satellite blisters. To quantitatively assess the size effect of the vdW process zone, we compare the numerical solutions to CZM to the approximate solutions to GTM in Fig. 8a. We introduce an error function defined as Error (%) = (approximate solution to GTM/numerical result to CZM-1)×100 (%) to identify the GTM-to-CZM transition. Fig. 8b illustrates the error distributions as a function of H at different

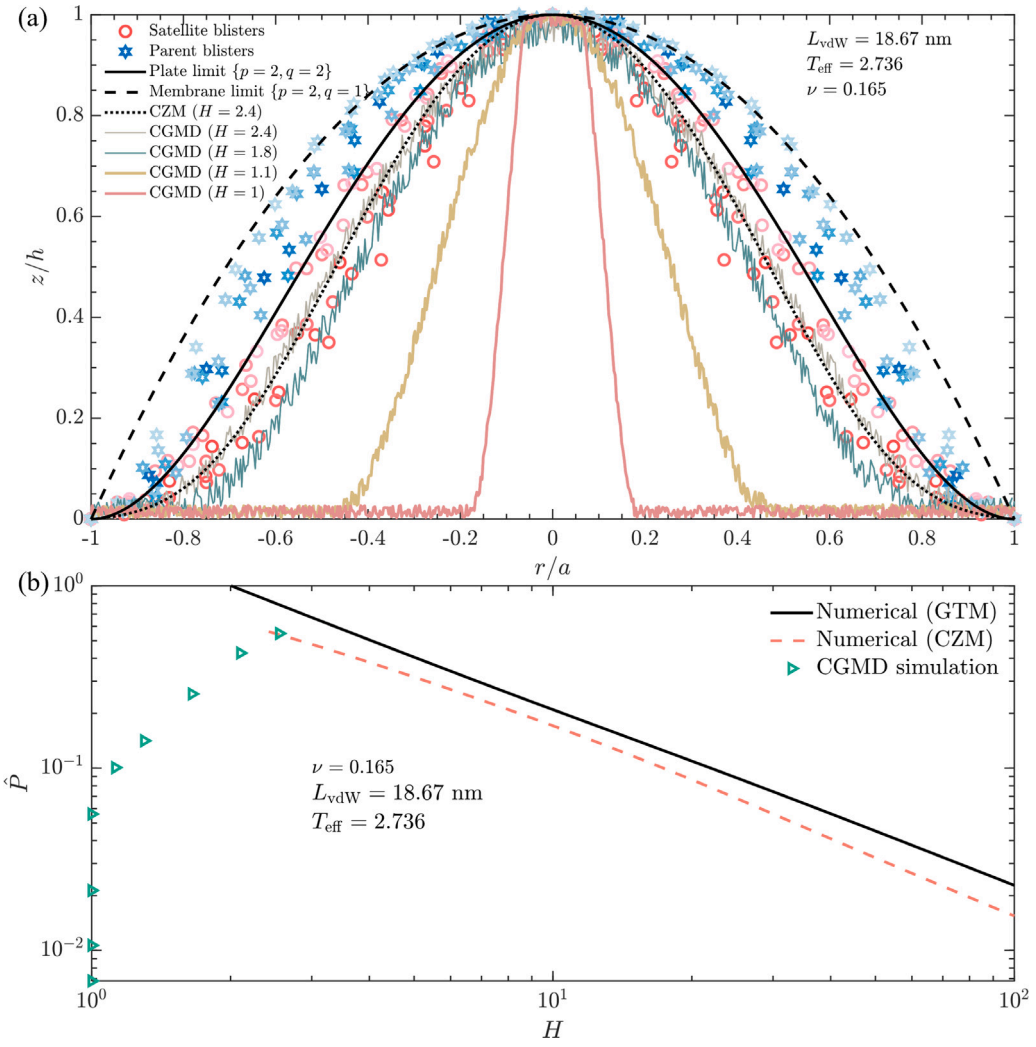


Fig. 9. (a) Fig. 2a replotted with numerical solutions to CZM with $H = 2.4$ (the dotted curve) and CGMD simulation results with various H. (b) Normalized blister pressure vs. normalized height obtained by numerical solutions to GTM (the solid curve) and CZM (the dashed curve) as well as CGMD simulations (markers).

values of T_{eff}, which is the only controlling parameter, besides ν, in the BVP based on the CZM. It can be observed that the error decreases as H increases, indicating that the size effect of the vdW process zone decreases as the central height of the blister increases. In this case, we define the GTM-to-CZM transition point as the point where the error reaches approximately 10%. Fig. 8c presents the dependence of the critical central height H_c of the GTM-to-CZM transition on T_{eff}. By fitting the numerical results, one obtains

$$H_c \approx 1 + 6.176 T_{\text{eff}}^{1/3}. \tag{27}$$

Based on this results, we conclude that the GTM is applicable to 2D crystal blisters with heights greater than the critical height ($H > H_c$), whereas the CZM is applicable to blisters with heights less than the critical height ($H < H_c$). For blisters at the 11LG/SiO_2 interface, the critical height is approximately $h_c \approx 3$ nm, as indicated by Eq. (27). This finding explains why the experimentally measured deflections of satellite blisters are lower than those predicted by plate theory, as depicted in Fig. 2a.

In addition to the numerical study, we conducted CGMD simulations based on the CZM to investigate ultra-shallow blisters with heights of only a few ångströms. We also conducted an annealing process in the CGMD simulations to validate that the blister system is in a steady state and has reached the global minimum (see details in Appendix D). As illustrated in Fig. 7, the results of the CGMD simulations, along with the numerical solutions to CZM, agree with the experimental measurements for satellite blisters. However, for smaller blistering volumes, the CGMD simulations surprisingly reveal an inversely proportional relationship between the aspect ratio and the blister radius. Upon analyzing blister profiles obtained from the CGMD simulations (refer to Figs. D.1–D.2), we discover

Table 1
A summary of the criteria of the plate-to-membrane transition, the GTM-to-CZM transition, and the liquid-to-monolayer-lattice transition for 2D crystal blisters. Here, δ_0, $t_{\text{eff}} = \sqrt{D/E_{2D}}$ and h denote the equilibrium vdW distance at 2D crystal-substrate interface, the effective thickness of the 2D crystal, and the blister central height, respectively.

	Pancake-like profile	Plate-like profile	Membrane-like profile
GTM	N/A	$\delta_0 + 6.18t_{\text{eff}}^{1/3}\delta_0^{2/3} < h < 5.37t_{\text{eff}}$	$h > \delta_0 + 6.18t_{\text{eff}}^{1/3}\delta_0^{2/3}$ & $h > 5.37t_{\text{eff}}$
CZM	N/A	$h < \delta_0 + 6.18t_{\text{eff}}^{1/3}\delta_0^{2/3}$ & $h < 5.37t_{\text{eff}}$	$5.37t_{\text{eff}} < h < \delta_0 + 6.18t_{\text{eff}}^{1/3}\delta_0^{2/3}$
CGMD	$h = \delta_0$	N/A	N/A

a limiting blister height corresponding to a single molecular layer of the confined substances, i.e., $H = 1$. Consequently, green dashed curves representing $H = 1$ are plotted in Fig. 7, which is consistent with the CGMD simulation outcomes for ultra-shallow blisters.

This exotic trend originates from a new mechanism breaking away from continuum theories, namely the transition of confined substances from an amorphous liquid state to a monolayer lattice configuration. Previous studies on monolayer 2D crystals have revealed a similar phenomenon, indicating that the phase state of confined substances is highly influenced by interactions among 2D crystals, interfacial substances, and substrates (Lee et al., 2012; Iakovlev et al., 2017; Bampoulis et al., 2018; Villarreal et al., 2021). When the number of molecules of the confined substances decreases, the interactions between graphene/substrate and confined substances as well as those among confined substances, give way to the interactions between graphene and substrate. This leads to the formation of pancake-like 2D crystal blisters that have a height equal to the height of a single molecular layer of the confined substances arranged in monolayer lattices. It is worth noting that external factors such as temperature and pressure may also affect the structure of the confined substances.

In summary, Fig. 2a, which depicts the blister morphology, has been updated as Fig. 9a by including the numerical solution to CZM with $H = 2.4$ and the CGMD simulation results with $H = 2.4, 1.8, 1.1, 1$. The good agreement between the numerical and simulation results at $H = 2.4$ suggests that both studies employed the same set of material and interfacial properties (see details in Appendix D). Moreover, as the blistering volume decreases, a transition from the dome shape to the pancake shape can be observed. Fig. 9b depicts the relationships between the normalized pressure and the normalized height, as determined by numerical solutions to CZM and GTM, as well as by CGMD simulation results. The blister pressure predicted by both the CZM and the GTM decreases as the central height increases. However, the GTM overestimates the pressure of a 2D crystal blister at a specific central height compared to the CZM. In contrast, the CGMD simulation results demonstrate that the pressure of ultra-shallow blisters decreases with decreasing central height initially and continues to decrease with decreasing blistering volume when the central height reaches the limiting value corresponding to one molecular layer of confined substances.

5. Conclusions

In this work, we fabricated nanoblisters confined between MLG and SiO_2 substrates through mechanical exfoliation. With the aid of AFM, we observed parent-satellite blister patterns and discovered that although the aspect ratio of the parent blisters is size-independent, the aspect ratio of the satellite blisters is size-dependent. To capture the shape characteristics of 2D crystal blisters, a Griffith-type model (GTM) has been established first. It elucidates that the spontaneous formation of 2D crystal blisters is governed by the interplay between the stretching and bending energies of the bulged 2D crystal, the change of interfacial energy, and the interfacial sliding. An approximate analytical solution (Eq. (17)) has been proposed, which agrees well with the numerical solutions to the GTM. The plate-to-membrane transition points have been identified given the effective thickness and a certain adhesive number.

The blister aspect ratio predicted by the GTM agrees well with experimental measurements for relatively tall blisters but broke down in shallow blisters. It suggests that for shallow blisters, such as the satellite nanoblisters, continuous vdW interactions between the bulged 2D crystal and the substrate have to be considered. We thus established a cohesive zone model (CZM) to investigate the shape characteristics of nanoblisters whose radii are comparable to the size of the vdW process zone. Our numerical solutions agree well with the experimental measurements of the satellite nanoblisters. It indicates that, instead of the GTM, the shallow nanoblisters are simultaneously governed by the CZM and the plate-like MLG. Through numerical study, the dependence of the critical blister height for the GTM-to-CZM transition on the effective thickness is revealed by Eq. (27).

We performed CGMD simulations as the CZM encountered difficulties in finding numerical solutions for ultra-shallow blisters with heights of a few ångströms. Through CGMD simulations, a limiting blister height corresponding to a single molecular layer of confined substances was observed, which indicates the formation of a monolayer lattice configuration within such ultra-shallow blisters. It further suggests that confined substances in ultra-shallow blisters would first expand laterally with a monolayer lattice configuration and then grow in height to form a dome shape with increasing volume.

Ultimately, the criteria of the plate-to-membrane transition, the GTM-to-CZM transition, and the liquid-to-monolayer-lattice transition is summarized in Table 1 as a practical guideline for choosing the correct models for 2D crystal blisters.

CRediT authorship contribution statement

Yifan Rao: Conceptualization, Methodology, Software, Formal analysis, Investigation, Writing – original draft. **Eunbin Kim:** Conceptualization, Formal analysis, Investigation , Writing – original draft. **Zhaohe Dai:** Conceptualization, Formal analysis, Investigation, Writing – review & editing. **Jinlong He:** Investigation, Resources , Writing – original draft. **Ying Li:** Resources, Funding acquistion, Writing – review & editing. **Nanshu Lu:** Validation, Supervision, Project administration, Funding acquisition, Writing – review & editing.

Declaration of competing interest

The authors declare that they have no known competing financial interests or personal relationships that could have appeared to influence the work reported in this paper.

Data availability

Data will be made available on request.

Acknowledgments

Taking Prof. Yonggang Huang as a respected role model, a lifelong mentor, and a caring friend, we wish Prof. Huang a very happy 60th birthday and all the best in everything. Y. R. acknowledges the Eugene A. Ripperger Scholarship at the University of Texas of Austin. Y.L. would like to thank the support from the US National Science Foundation under Grants 1755779, 1762661 and 1934829, as well as 3M's Non-Tenured Faculty Award.

Appendix A. Profile measurements of 2D crystal blisters

Fig. A.1 a-(i) and b-(i) depict AFM images of the same parent-satellite blister system on Day 0 and Day 100 after fabrication, respectively. To evaluate the roundness of the parent blister, we made eight cuts that pass through the apex of the parent blister with a 22.5-degree angle between adjacent ones. AFM height profiles along the corresponding directions of cuts measured on Day 0 and Day 100 after fabrication are shown in Fig. A.1 a-(ii) and b-(ii), respectively. The AFM height profiles are almost identical, indicating that the parent blister maintains a round shape during the 100-day period. The diameter D and the central height h of the parent blister measured along the corresponding directions of cuts are tabulated at the bottom of Fig. A.1. By comparing the values, we identified the directions of the longest and shortest axes of the parent blister, which are marked in Fig. 1 c: for the parent blister on Day 0 after fabrication, cut 1 is the longest axis and cut 4 is the shortest axis; for the parent blister on Day 100 after fabrication, cut 7 is the longest axis and cut 3 is the shortest axis. In addition, we used the same method, starting from the apex of each satellite blister, to measure the profiles of the satellite blisters and prove their round shapes. It is worth noting that the diameter of the blister is determined by averaging the diameters measured along the longest and shortest axes in this study.

Appendix B. Derivation of adhesive boundary condition

The total free energy of a 2D crystal blister yields a functional of the form

$$\Pi = \int_0^a \pounds_\alpha dr + \int_a^\infty \pounds_\beta dr, \tag{B.1}$$

with

$$\begin{cases} \pounds_\alpha = 2\pi r[\psi_\alpha + \Delta\gamma - \Delta p w] \\ \pounds_\beta = 2\pi r \psi_\beta \end{cases}, \tag{B.2}$$

where ψ_α and ψ_β are the elastic energy densities evaluated at the inner and the outer sides of blisters, respectively.

To satisfy the compatibility of deformations across the blister edge, there are

$$u(a^-) = u(a^+), w(a^-) = w(a^+) = 0, w'(a^-) = w'(a^+) = 0, w''(a^+) = 0, \tag{B.3}$$

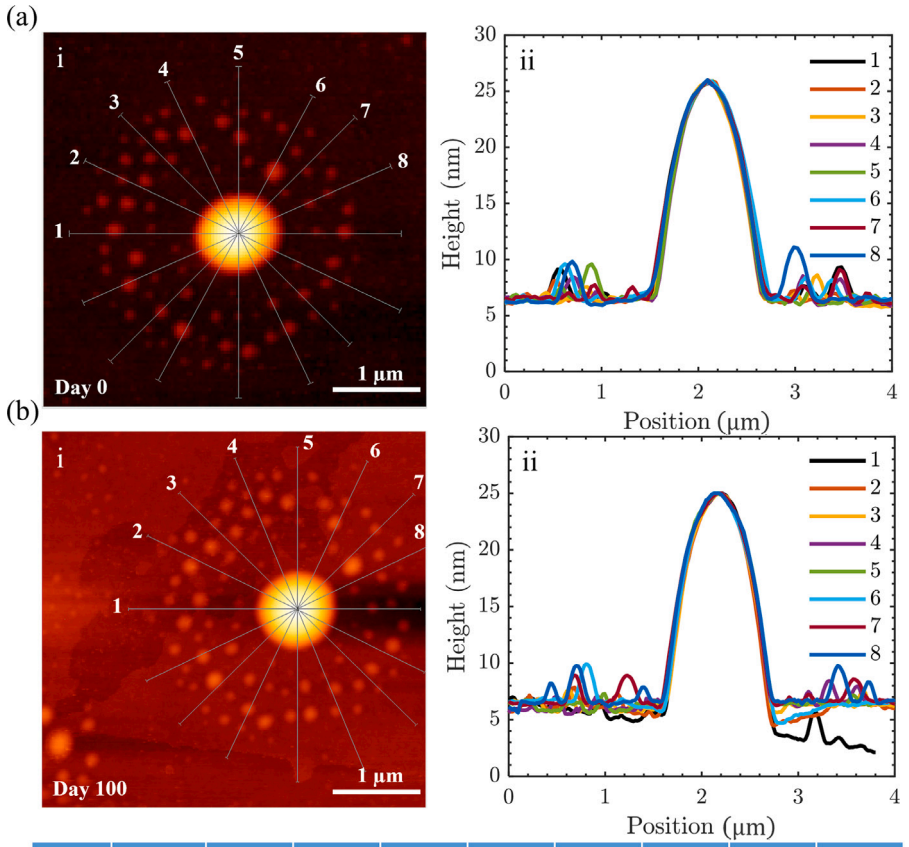
where a^- and a^+ represent the inner and the outer sides of $r = a$, respectively.

Based on the assumption of interfacial frictionless, there are

$$\begin{cases} \psi_\alpha = \frac{D}{2}[w''^2 + 2\nu w'' \frac{w'}{r} + \frac{w'^2}{r^2}] + \frac{E_{2D}}{2(1-\nu^2)}[(u' + \frac{w'^2}{2})^2 + \frac{u^2}{r^2} + 2\nu(u' + \frac{w'^2}{2})\frac{u}{r}] \\ \psi_\beta = \frac{E_{2D}}{2(1-\nu^2)}[u'^2 + \frac{u^2}{r^2} + 2\nu u' \frac{u}{r}] \end{cases}. \tag{B.4}$$

At equilibrium, the variation $\delta\Pi$ must vanish with respect to arbitrary but kinematically admissible variables δa, δu, and δw. Therefore, the variation of Eq. (B.1) leads to

$$\delta\Pi = \int_0^a \delta\pounds_\alpha dr + \int_a^\infty \delta\pounds_\beta dr + \pounds_\alpha \delta a - \pounds_\beta \delta a = 0. \tag{B.5}$$



Day		1	2	3	4	5	6	7	8
D 0	D (μm)	1.276	1.197	1.214	1.190	1.193	1.241	1.262	1.238
	h (nm)	19.57	19.66	19.53	19.48	19.57	19.48	19.48	19.40
D 100	D (μm)	1.159	1.141	1.114	1.134	1.159	1.193	1.2	1.176
	h (nm)	19.48	19.61	19.21	18.79	18.53	19.18	18.75	18.45

Fig. A.1. (a) (i) AFM image and (ii) AFM height profiles along the corresponding directions of cuts labeled in (i) of a single parent-satellite blister system on Day 0 after fabrication. (b) (i) AFM image and (ii) AFM height profiles along the corresponding directions of cuts labeled in (i) of a single parent-satellite blister system on Day 100 after fabrication. The cuts go through the apex of the parent blister with a 22.5-degree angle between adjacent ones. The diameters D and the central heights h of the parent blister measured along the corresponding directions of cuts on both Day 0 and Day 100 after fabrication are listed in the table.

Plugging Eqs. (B.2)–(B.4) into Eq. (B.5), one obtains

$$\begin{aligned}&\int_0^a [\frac{\partial \pounds_\alpha}{\partial u} - \frac{\mathrm{d}}{\mathrm{d}r}(\frac{\partial \pounds_\alpha}{\partial u'})] + [\frac{\partial \pounds_\alpha}{\partial w} - \frac{\mathrm{d}}{\mathrm{d}r}(\frac{\partial \pounds_\alpha}{\partial w'}) + \frac{\mathrm{d}^2}{\mathrm{d}r^2}(\frac{\partial \pounds_\alpha}{\partial w''})]dr \\ &+ \int_a^\infty [\frac{\partial \pounds_\beta}{\partial u} - \frac{\mathrm{d}}{\mathrm{d}r}(\frac{\partial \pounds_\beta}{\partial u'})]dr \\ &+ [\pounds_\alpha(a^-) - \pounds_\beta(a^+) - w''(a^-)\frac{\partial \pounds_\alpha(a^-)}{\partial w''}]\delta a \\ &+ \frac{\partial \pounds_\alpha(a^-)}{\partial u'}\delta u(a^-) - \frac{\partial \pounds_\alpha(a^+)}{\partial u'}\delta u(a^+) = 0\end{aligned} \tag{B.6}$$

The first term of Eq. (B.6) yields two governing equations, Eqs. (6) and (7). The second term yields an in-plane equilibrium equation at the outer side of the blister, given by

$$u'' + \frac{u'}{r} - \frac{u}{r^2} = 0 \qquad (a < r < \infty), \tag{B.7}$$

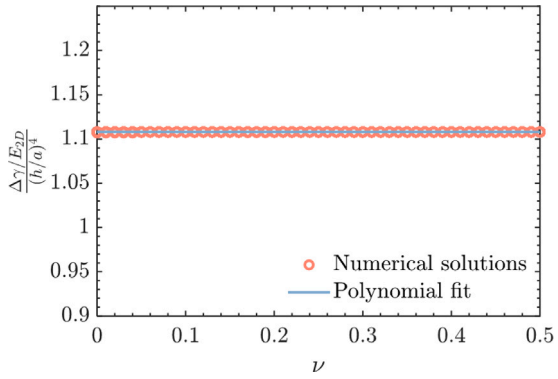


Fig. C.1. Dependence of $\frac{\Delta\gamma/E_{2D}}{(h/a)^4}$ on ν for 2D crystal blisters at the frictionless interface under various Δp in the membrane limit.

which leads to $u(r) = \frac{C}{r}$, where C is an unknown constant. The third term gives the adhesive boundary condition, Eq. (9), and the fourth term leads to

$$u'(a^-) = u'(a^+). \tag{B.8}$$

Using Eq. (B.3), the solution to Eqs. (B.7), and (B.8), one obtains

$$\begin{aligned} u'(a^-) &= -\frac{C}{a^2} \\ u(a^-) &= \frac{C}{a} \\ w'(a^-) &= 0. \end{aligned} \tag{B.9}$$

By plugging Eq. (B.9) into Eq. (3), one obtains

$$\epsilon_r(a^-) + \epsilon_\theta(a^-) = 0. \tag{B.10}$$

Thus, the supplementary boundary condition, Eq. (10), is derived by substituting Eq. (B.10) into Eq. (5).

Appendix C. Extracted prefactor in the membrane limit

By setting the bending stiffness term to zero in Eqs. (6) and (7), the governing equations for 2D crystal blisters in the membrane limit are simplified as

$$\begin{cases} [\psi, w] + \Delta p = 0 \\ \nabla^4\psi + \frac{E_{2D}}{2}[w, w] = 0 \end{cases}. \tag{C.1}$$

The corresponding boundary conditions are given by

$$\begin{cases} w'(0) = 0 \\ w(a) = 0 \\ u(0) = \frac{1}{E_{2D}}(\psi''(r) - \nu\frac{\psi'(r)}{r})|_{r=0} = 0 \\ u'(a^-) + \frac{u(a^-)}{a} = 0 \\ \frac{1}{2}w'^2(a^-) - \frac{\Delta\gamma a}{\psi'(a^-)} = 0 \end{cases}. \tag{C.2}$$

Here, the fourth boundary condition is obtained from Eqs. (B.8) and (B.9), and the fifth boundary condition is derived by plugging Eq. (4) into Eq. (8). The BVP in the membrane limit can be solved numerically using the built-in solver bvp4c in MATLAB.

To validate the scaling law $\Delta\gamma \propto E_{2D}h^4/a^4$ and extract the corresponding prefactor, we vary the pressure difference Δp during numerical calculations to obtain blister profiles with different radii and central heights under a prescribed parameter group $\{E_{2D}, \Delta\gamma, \nu\}$. We then tune Poisson's ratio ν to investigate the influence of the compressibility of 2D crystals on the value of the prefactor. Fig. C.1 shows the dependence of $\Delta\gamma/[E_{2D}(h/a)^4]$ on ν under various Δp. The prefactor is identified as 1.108 through polynomial fitting using MATLAB coding, and it is used in Eqs. (16) and (17).

Appendix D. Coarse-grained molecular dynamics (CGMD) simulation method

We performed CGMD simulations to study ultra-shallow blisters at the 11LG/SiO_2 interface using LAMMPS (Plimpton, 1995). A 200 nm X 200 nm square was used to simulate the 11LG with an interlayer distance of 3.46 Å, and it was placed on a flat and rigid SiO_2 substrate. After calibration, the equilibrium distance between the bottom layer of 11LG and SiO_2 was set as 0.4 nm. CGMD

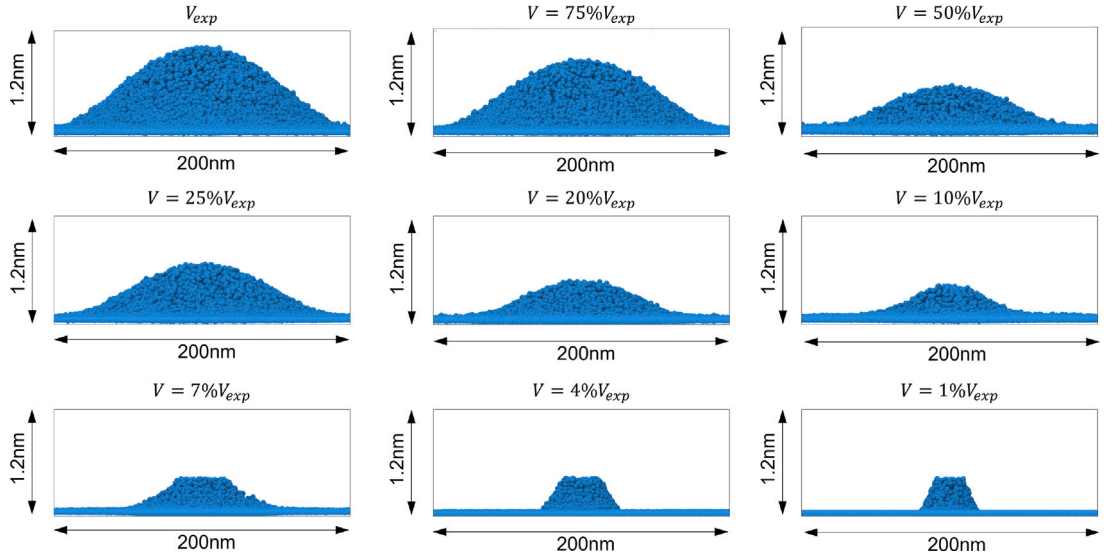


Fig. D.1. Atomistic snapshots of 2D crystal blister configurations given by CGMD simulations. The maximum volume of water molecules performed in simulations is identical to the minimum blistering volume measured in experiments $V_{exp} = 7.16 \times 10^{-24}$ m^3, and then the volume is reduced to 75%, 50%, 25%, 20%, 10%, 7%, 4%, and 1% of V_{exp}.

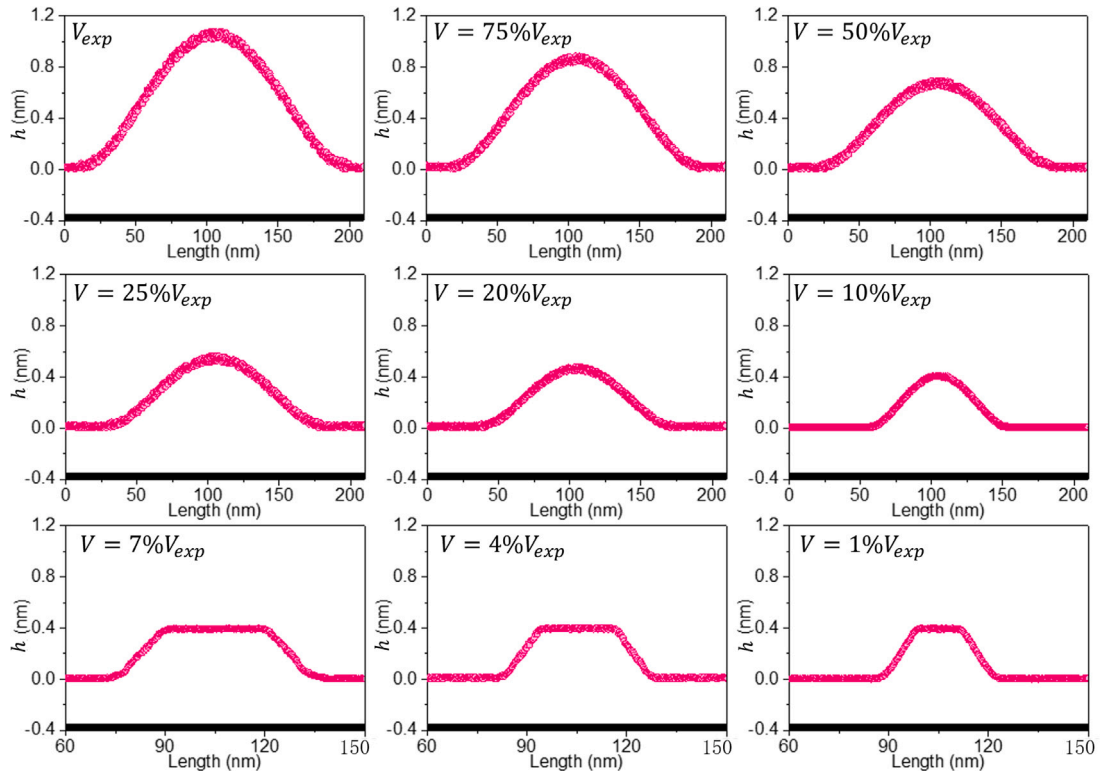


Fig. D.2. Height profiles of 2D crystal blisters given by CGMD simulations.

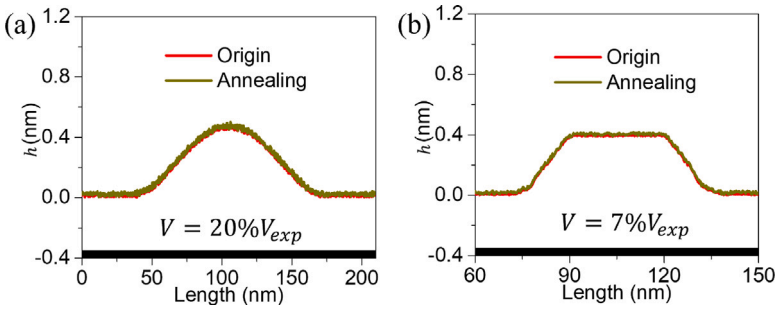


Fig. D.3. Height profiles of 2D crystal blisters given by CGMD simulations before and after annealing at (a) $V = 20\%V_{exp}$ and (b) $V = 7\%V_{exp}$, respectively.

simulations were conducted under the NVT ensemble at 300 K with an integration time step of 1.0 fs. A nose-Hoover thermostat was used to control the system temperature. Periodic boundary conditions were applied in three directions (x, y, and z) with box sizes of $\{x \sim 300$ nm, $y \sim 300$ nm, and $z \sim 100$ nm$\}$ to prevent interactions due to periodic images. At the start of the simulation, an empty block was generated between 11LG and SiO_2 substrate by pushing 11LG out from its center using a nanoindenter. Then, a certain number of water molecules were deposited into this block, and a relaxation time of 10 ns was conducted to form a blister-like shape. The system reached an equilibrium state when the profile and the potential energy showed no statistically significant differences. We extracted mechanical information (i.e., height, volume, radius, pressure, etc.) from CGMD simulations by evenly sampling 100 snapshots within 2 ns of relaxation.

It is essential to calibrate the molecular interactions when implementing CGMD simulations. Therefore, we used the calibrated CG potential (Ruiz et al., 2015; Li, 2016), including bond, angle, dihedral, and non-bonded interactions, to model the carbon–carbon interaction of graphene. An improved CG MARTINI 3 model (Souza et al., 2021) was used to describe interactions among water molecules, which has been shown to accurately predict water density, enthalpy of vaporization, and surface tension (Yesudasan, 2020). We modeled the rigid substrate interacting with both water molecules and graphene as a fictitious surface (Wang et al., 2016). The interactions between graphene and water were described by the standard Lennard-Jones potential model, based on previous first-principle calculations (Ma et al., 2011) and other calibrated simulations (Werder et al., 2003; Sanchez et al., 2018).

In the first study case, a total volume of 7.16×10^{-24} m^3 of water molecules was implanted at the 11LG/SiO_2 interface in the CGMD simulation, based on experimental measurements. Figs. 7 and 9 demonstrate good agreement between the CGMD simulation result and the numerical solution to CZM, indicating consistent material and interfacial properties applied to both calculations. Subsequently, the volume of water molecules was reduced to 75%, 50%, 25%, 20%, 10%, 7%, 4%, and 1% of the maximum volume performed in CGMD simulations. The atomistic snapshots of these blister configurations obtained by CGMD simulations are shown in Fig. D.1, and the corresponding height profiles are displayed in Fig. D.2. Upon reduction in the number of water molecules, a limiting blister height equivalent to the height of a single layer of water molecules was observed.

To ensure that the blister system is in a steady state and has reached a global minimum, we conducted an annealing process on two simulation systems with 20% and 7% remaining water, respectively. Five annealing cycles were performed on each system, which involved heating the system up from 300 K to 373 K within 1 ns, relaxing it at 373 K for 1 ns, and finally cooling it down to 300 K in 1 ns. Subsequently, the system was relaxed for 1 ns at 300 K in NVT. For production runs, the structures were further equilibrated for 10 ns in NVT at 300 K, with a reduced time step of 0.5 fs. The blister configuration was obtained by evenly sampling 100 snapshots within the last 2 ns of relaxation. The resulting blister profiles after annealing were compared to the original profile, as shown in Fig. D.3. The comparison revealed a good agreement between the two profiles, indicating that the system is indeed in a steady state and has reached a global minimum.

References

Aitken, Z.H., Huang, R., 2010. Effects of mismatch strain and substrate surface corrugation on morphology of supported monolayer graphene. J. Appl. Phys. 107 (12), 123531.

Akinwande, D., Brennan, C.J., Bunch, J.S., Egberts, P., Felts, J.R., Gao, H., Huang, R., Kim, J.-S., Li, T., Li, Y., et al., 2017. A review on mechanics and mechanical properties of 2D materials—Graphene and beyond. Extreme Mech. Lett. 13, 42–77.

Ares, P., Wang, Y.B., Woods, C.R., Dougherty, J., Fumagalli, L., Guinea, F., Davidovitch, B., Novoselov, K.S., 2021. Van der Waals interaction affects wrinkle formation in two-dimensional materials. Proc. Natl. Acad. Sci. 118 (14), e2025870118.

Bampoulis, P., Sotthewes, K., Dollekamp, E., Poelsema, B., 2018. Water confined in two-dimensions: Fundamentals and applications. Surf. Sci. Rep. 73 (6), 233–264.

Blundo, E., Yildirim, T., Pettinari, G., Polimeni, A., 2021. Experimental adhesion energy in van der waals crystals and heterostructures from atomically thin bubbles. Phys. Rev. Lett. 127 (4), 046101.

Brennan, C.J., Koul, K., Lu, N., Yu, E.T., 2020. Out-of-plane electromechanical coupling in transition metal dichalcogenides. Appl. Phys. Lett. 116 (5), 053101.

Dai, Z., Hou, Y., Sanchez, D.A., Wang, G., Brennan, C.J., Zhang, Z., Liu, L., Lu, N., 2018. Interface-governed deformation of nanobubbles and nanotents formed by two-dimensional materials. Phys. Rev. Lett. 121 (26), 266101.

Dai, Z., Lu, N., 2021. Poking and bulging of suspended thin sheets: Slippage, instabilities, and metrology. J. Mech. Phys. Solids 149, 104320.

Dai, Z., Rao, Y., Lu, N., 2022. Two-dimensional crystals on adhesive substrates subjected to uniform transverse pressure. Int. J. Solids Struct. 257, 111829.

Dai, Z., Sanchez, D.A., Brennan, C.J., Lu, N., 2020. Radial buckle delamination around 2D material tents. J. Mech. Phys. Solids 137, 103843.

De Palma, A.C., Cossio, G., Jones, K., Quan, J., Li, X., Yu, E.T., 2020. Strain-dependent luminescence and piezoelectricity in monolayer transition metal dichalcogenides. J. Vac. Sci. Technol. B 38 (4), 042205.
Fang, Z., Dai, Z., Wang, B., Tian, Z., Yu, C., Chen, Q., Wei, X., 2022. Pull-to-peel of two-dimensional materials for the simultaneous determination of elasticity and adhesion. Nano Lett..
Gao, W., Huang, R., 2011. Effect of surface roughness on adhesion of graphene membranes. J. Phys. D: Appl. Phys. 44 (45), 452001.
Geim, A.K., Grigorieva, I.V., 2013. Van der Waals heterostructures. Nature 499 (7459), 419–425.
Gibertini, M., Koperski, M., Morpurgo, A.F., Novoselov, K.S., 2019. Magnetic 2D materials and heterostructures. Nature Nanotechnol. 14 (5), 408–419.
Griffith, A.A., 1921. VI. The phenomena of rupture and flow in solids. Philos. Trans. R. Soc. A 221 (582–593), 163–198.
Gupta, A., Chen, G., Joshi, P., Tadigadapa, S., Eklund, P., 2006. Raman scattering from high-frequency phonons in supported n-graphene layer films. Nano Lett. 6 (12), 2667–2673.
Iakovlev, E., Zhilyaev, P., Akhatov, I., 2017. Atomistic study of the solid state inside graphene nanobubbles. Sci. Rep. 7 (1), 17906.
Ishigami, M., Chen, J., Cullen, W., Fuhrer, M., Williams, E., 2007. Atomic structure of graphene on SiO2. Nano Lett. 7 (6), 1643–1648.
Jain, A., Bharadwaj, P., Heeg, S., Parzefall, M., Taniguchi, T., Watanabe, K., Novotny, L., 2018. Minimizing residues and strain in 2D materials transferred from PDMS. Nanotechnology 29 (26), 265203.
Jang, H., Sel, K., Kim, E., Kim, S., Yang, X., Kang, S., Ha, K.-H., Wang, R., Rao, Y., Jafari, R., et al., 2022. Graphene e-tattoos for unobstructive ambulatory electrodermal activity sensing on the palm enabled by heterogeneous serpentine ribbons. Nature Commun. 13 (1), 1–13.
Khestanova, E., Guinea, F., Fumagalli, L., Geim, A., Grigorieva, I., 2016. Universal shape and pressure inside bubbles appearing in van der Waals heterostructures. Nature Commun. 7 (1), 1–10.
Koskinen, P., Kit, O.O., 2010. Approximate modeling of spherical membranes. Phys. Rev. B 82 (23), 235420.
Lee, M.J., Choi, J.S., Kim, J.-S., Byun, I.-S., Lee, D.H., Ryu, S., Lee, C., Park, B.H., 2012. Characteristics and effects of diffused water between graphene and a SiO 2 substrate. Nano Res. 5, 710–717.
Levy, N., Burke, S., Meaker, K., Panlasigui, M., Zettl, A., Guinea, F., Neto, A.C., Crommie, M.F., 2010. Strain-induced pseudo–magnetic fields greater than 300 tesla in graphene nanobubbles. Science 329 (5991), 544–547.
Li, Y., 2016. Reversible wrinkles of monolayer graphene on a polymer substrate: toward stretchable and flexible electronics. Soft Matter 12 (13), 3202–3213.
Lin, H., Fraser, S., Hong, M., Chhowalla, M., Li, D., Jia, B., 2020. Near-perfect microlenses based on graphene microbubbles. Adv. Photonics 2 (5), 055001.
Lloyd, D., Liu, X., Boddeti, N., Cantley, L., Long, R., Dunn, M.L., Bunch, J.S., 2017. Adhesion, stiffness, and instability in atomically thin MoS2 bubbles. Nano Lett. 17 (9), 5329–5334.
Ma, X., Liu, L., Zhang, Z., Wei, Y., 2022. Bending stiffness of circular multilayer van der Waals material sheets. J. Appl. Mech. 89 (3), 031011.
Ma, J., Michaelides, A., Alfe, D., Schimka, L., Kresse, G., Wang, E., 2011. Adsorption and diffusion of water on graphene from first principles. Phys. Rev. B 84 (3), 033402.
Mak, K.F., Shan, J., 2016. Photonics and optoelectronics of 2D semiconductor transition metal dichalcogenides. Nat. Photonics 10 (4), 216–226.
Mansfield, E.H., 2005. The Bending and Stretching of Plates. p. 240.
Novoselov, K.S., Geim, A.K., Morozov, S.V., Jiang, D.-e., Zhang, Y., Dubonos, S.V., Grigorieva, I.V., Firsov, A.A., 2004. Electric field effect in atomically thin carbon films. Science 306 (5696), 666–669.
Novoselov, K., Mishchenko, o.A., Carvalho, o.A., Castro Neto, A., 2016. 2D materials and van der Waals heterostructures. Science 353 (6298), aac9439.
Novoselov, K., Neto, A.C., 2012. Two-dimensional crystals-based heterostructures: materials with tailored properties. Phys. Scr. 2012 (T146), 014006.
Pizzocchero, F., Gammelgaard, L., Jessen, B.S., Caridad, J.M., Wang, L., Hone, J., Bøggild, P., Booth, T.J., 2016. The hot pick-up technique for batch assembly of van der Waals heterostructures. Nature Commun. 7 (1), 1–10.
Plimpton, S., 1995. Fast parallel algorithms for short-range molecular dynamics. J. Comput. Phys. 117 (1), 1–19.
Purdie, D., Pugno, N., Taniguchi, T., Watanabe, K., Ferrari, A., Lombardo, A., 2018. Cleaning interfaces in layered materials heterostructures. Nature Commun. 9 (1), 1–12.
Rao, Y., Qiao, S., Dai, Z., Lu, N., 2021. Elastic wetting: Substrate-supported droplets confined by soft elastic membranes. J. Mech. Phys. Solids 151, 104399.
Rosenberger, M.R., Chuang, H.-J., McCreary, K.M., Hanbicki, A.T., Sivaram, S.V., Jonker, B.T., 2018. Nano-“squeegee” for the creation of clean 2D material interfaces. ACS Appl. Mater. Interfaces 10 (12), 10379–10387.
Ruiz, L., Xia, W., Meng, Z., Keten, S., 2015. A coarse-grained model for the mechanical behavior of multi-layer graphene. Carbon 82, 103–115.
Sanchez, D.A., Dai, Z., Lu, N., 2021. 2D material bubbles: Fabrication, characterization, and applications. Trends Chem. 3 (3), 204–217.
Sanchez, D.A., Dai, Z., Wang, P., Cantu-Chavez, A., Brennan, C.J., Huang, R., Lu, N., 2018. Mechanics of spontaneously formed nanoblisters trapped by transferred 2D crystals. Proc. Natl. Acad. Sci. 115 (31), 7884–7889.
Sonde, S., Giannazzo, F., Raineri, V., Rimini, E., 2009. Dielectric thickness dependence of capacitive behavior in graphene deposited on silicon dioxide. J. Vac. Sci. Technol. B 27 (2), 868–873.
Souza, P.C., Alessandri, R., Barnoud, J., Thallmair, S., Faustino, I., Grünewald, F., Patmanidis, I., Abdizadeh, H., Bruininks, B.M., Wassenaar, T.A., et al., 2021. Martini 3: a general purpose force field for coarse-grained molecular dynamics. Nature Methods 18 (4), 382–388.
Stolyarova, E., Stolyarov, D., Bolotin, K., Ryu, S., Liu, L., Rim, K., Klima, M., Hybertsen, M., Pogorelsky, I., Pavlishin, I., et al., 2009. Observation of graphene bubbles and effective mass transport under graphene films. Nano Lett. 9 (1), 332–337.
Uwanno, T., Hattori, Y., Taniguchi, T., Watanabe, K., Nagashio, K., 2015. Fully dry PMMA transfer of graphene on h-BN using a heating/cooling system. 2D Mater. 2 (4), 041002.
Vasu, K., Prestat, E., Abraham, J., Dix, J., Kashtiban, R., Beheshtian, J., Sloan, J., Carbone, P., Neek-Amal, M., Haigh, S., et al., 2016. Van der Waals pressure and its effect on trapped interlayer molecules. Nature Commun. 7 (1), 1–6.
Villarreal, R., Lin, P.-C., Faraji, F., Hassani, N., Bana, H., Zarkua, Z., Nair, M.N., Tsai, H.-C., Auge, M., Junge, F., et al., 2021. Breakdown of universal scaling for nanometer-sized bubbles in graphene. Nano Lett. 21 (19), 8103–8110.
Wang, G., Dai, Z., Wang, Y., Tan, P., Liu, L., Xu, Z., Wei, Y., Huang, R., Zhang, Z., 2017. Measuring interlayer shear stress in bilayer graphene. Phys. Rev. Lett. 119 (3), 036101.
Wang, P., Gao, W., Cao, Z., Liechti, K.M., Huang, R., 2013. Numerical analysis of circular graphene bubbles. J. Appl. Mech. 80 (4), 040905.
Wang, P., Liechti, K.M., Huang, R., 2016. Snap transitions of pressurized graphene blisters. J. Appl. Mech. 83 (7).
Wang, W., Ma, X., Dai, Z., Zhang, S., Hou, Y., Wang, G., Li, Q., Zhang, Z., Wei, Y., Liu, L., 2022. Mechanical behavior of blisters spontaneously formed by multilayer 2D materials. Adv. Mater. Interfaces 9 (12), 2101939.
Werder, T., Walther, J.H., Jaffe, R., Halicioglu, T., Koumoutsakos, P., 2003. On the water- carbon interaction for use in molecular dynamics simulations of graphite and carbon nanotubes. J. Phys. Chem. B 107 (6), 1345–1352.
Xue, Z., Chen, G., Wang, C., Huang, R., 2022. Peeling and sliding of graphene nanoribbons with periodic van der Waals interactions. J. Mech. Phys. Solids 158, 104698.
Yang, T., Jiang, X., Huang, Y., Tian, Q., Zhang, L., Dai, Z., Zhu, H., 2022. Mechanical sensors based on two-dimensional materials: Sensing mechanisms, structural designs and wearable applications. Iscience 103728.
Yesudasan, S., 2020. Extended MARTINI water model for heat transfer studies. Mol. Phys. 118 (13), e1692151.
Yi, M., Shen, Z., 2015. A review on mechanical exfoliation for the scalable production of graphene. J. Mater. Chem. A 3 (22), 11700–11715.
Yue, K., Gao, W., Huang, R., Liechti, K.M., 2012. Analytical methods for the mechanics of graphene bubbles. J. Appl. Phys. 112 (8), 083512.